Optics Letters

Terahertz metalens for generating multi-polarized focal points and images with uniform intensity distributions

Binbin Lu, Yefei Fu, Teng Zhang, Zuanming Jin, Xiaofei Zang,* and Yiming Zhu

Terahertz Technology Innovation Research Institute and Shanghai Key Lab of Modern Optical System, University of Shanghai for Science and Technology, No. 516 JunGong Road, Shanghai 200093, China
**xfzang@usst.edu.cn*

Received 23 January 2024; revised 11 March 2024; accepted 16 March 2024; posted 18 March 2024; published 16 April 2024

Metasurfaces have provided a flexible platform for designing ultracompact metalenses with unusual functionalities. However, traditional multi-foci metalenses are limited to generating circularly polarized (CP) or linearly polarized (LP) focal points, and the intensity distributions are always inhomogeneous/chaotical between the multiple focal points. Here, an inverse design approach is proposed to optimize the in-plane orientation of each meta-atom in a terahertz (THz) multi-foci metalens that can generate multi-polarized focal points with nearly uniform intensity distributions. As a proof-of-principle example, we numerically and experimentally demonstrate an inversely designed metalens for simultaneously generating multiple CP- and LP-based focal points with homogeneous intensity distributions, leading to a multi-polarized image (rather than the holography). Furthermore, the multi-channel and multi-polarized images consisting of multiple focal points with homogeneous intensity distributions are also numerically demonstrated. The unique approach for inversely designing multi-foci metalens that can generate multi-polarized focal points and images with uniform intensity distributions will enable potential applications in imaging and sensing.

https://doi.org/10.1364/OL.519605

Metasurfaces, which are the two-dimensional counterparts of metamaterials, enable unprecedented capabilities in the local manipulation of the light's amplitude, phase and polarization, leading to a variety of applications in the generalized Snell's law [1,2], polarization control and analysis [3–9], spin-Hall effects [10–13], light beam shaping [14,15], holograms [16–21], metalenses [22–30], etc. As a typical functional device, a multi-foci metalens can enable functionalities in the large field of view [31] and fully reconfigurable imaging [32] that are extremely challenging to achieve with conventional lenses. However, traditional multi-foci metalenses are mainly focused on the phase modulation, and thus, they are restricted to generating circularly polarized (CP) or linearly polarized (LP) focal points with inhomogeneous intensity distributions between the multiple focal points. A multi-foci metalens with the combined modulation of amplitude (intensity distributions) and phase and polarization (multiple polarization) of the incident beam is highly desired for generating multi-polarized focal points with high-accuracy intensity distributions, resulting in practical applications in imaging, polarization detecting, and biosensing.

Recently, inverse design methods, in which the optimization of structures (i.e., the length, width, and height) of each meta-atom provides a flexible design space for wavefront engineering, have been proposed to obtain high-accuracy functionalities [33–35]; e.g., a high performance and robust on-chip demultiplexer has been designed based on gradient descent methods [36]. The large-area metasurfaces have been designed via an inverse design method with the help of a locally periodic approximation [37]. The inverse design approach can be also applied to optimize metasurfaces to design high-quality devices such as multifunctional metagratings, light deflectors, and beam steering [38–40]. However, most of the devices with high-accuracy functionalities based on an inverse design are focused on topology optimization of structures (the optimization of the length, width, and height of each meta-atom). The optimization of the in-plane orientation of each meta-atom in a metasurface to realize high-accuracy functionlities has not attracted much attention yet.

In order to design a multi-foci metalens that can generate multi-polarized focal points and images with high-accuracy intensity distributions, an inverse design approach is proposed by automatically optimizing the amplitude of each meta-atom (which is translated into the global modulation of the total phase by optimizing the in-plane orientation of each meta-atom). The single- and dual-channel of multi-polarized images consisting of multi-polarized focal points with homogeneous intensity distributions are demonstrated. The simultaneous manipulation of phase, polarization, and intensity distributions of THz waves may open a new window for designing other flat devices with high-accuracy functionalities.

Figure 1(a) shows the schematic of a metalens that can generate multi-polarized focal points with high-accuracy intensity distributions. For the incidence of left-/right-handed circularly polarized (LCP/RCP) THz waves, a plethora of RCP/LCP focal points are generated, leading to the letters "V/*N*", respectively. Under the illumination of LP THz waves, a letter "W" with uniform intensity distributions between each focal point can be observed. In order to generate a variety of RCP/LCP focal points,

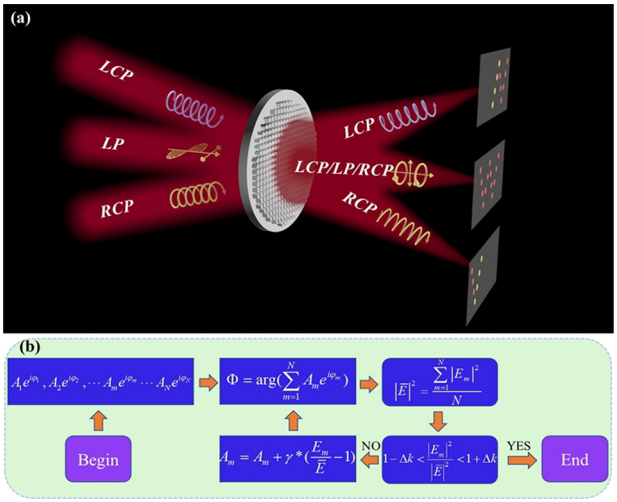

Fig. 1. (a) Schematic of a multi-foci metalens that can generate a multi-polarized image consisting of CP- and LP-based focal points with homogeneous intensity distributions. (b) Chart of an iterative algorithm for the inverse design of a multi-foci metalens.

the phase requirement for the designed metalens is governed by

$$\varphi_{LCP}(x,y) = \arg\left\{c_1 \exp\left[\sum_{i=1}^{N_1} A_i \left(\frac{2\pi}{\lambda}\sqrt{(x-x_i)^2+(y-y_i)^2+f_i^2} - f_i\right)\right]\right\}, \quad (1)$$

$$\varphi_{RCP}(x,y) = -\arg\left\{c_2 \exp\left[\sum_{j=1}^{N_2} A_j \left(\frac{2\pi}{\lambda}\sqrt{(x-x_j)^2+(y-y_j)^2+f_j^2} - f_j\right)\right]\right\}, \quad (2)$$

where λ (=428.5 μm) is the working wavelength and $f_{i/j}$ (=4 mm) is the focal length of the i^{th}/j^{th} focal points. ($x_{i/j}$, $y_{i/j}$, $f_{i/j}$) and $A_{i/j}$ are the corresponding focusing position and amplitude, respectively. C_1/C_2 is the amplitude and we assume $c_1 = c_2 = 1$. By overlapping a part of focal points from letters "V" and "*N*" with the identical amplitude, another letter "W" consisting of CP- and LP-based focal points can be obtained (for the incidence of LP THz waves), resulting in a multi-polarized image. The total phase requirement for the multi-polarized image can be expressed as follows:

$$\varphi_{LP}(x,y) = \arg[\exp(i\varphi_{LCP}(x,y)) + \exp(i\varphi_{RCP}(x,y))]. \quad (3)$$

When $A_i = A_j$ and $f_i = f_j$, the generated letter should be observed with a homogeneous field intensity distribution (in theory). However, all of the focal spots are focused at different positions (with a different numerical aperture for each focal point), resulting in the inhomogeneous intensity distributions between each focal point. To obtain the homogeneous intensity distributions, an iterative algorithm for the inverse design of a multifoci metalens is shown in Fig. 1(b). The initial amplitude of each focal point is selected as $A_i = A_j = 1$ (without the overlapping of LCP and RCP focal points) or 0.707 (in the overlapping position) ($i = 1 \ldots N_1$, $j = 1 \ldots N_2$, $N = N_1 + N_2$ and $m = 1 \ldots N$). The initial phase profile is $\Phi = \arg(\sum_{m=1}^{N} A_m e^{i\varphi_m})$ and the maximum intensity ($|E_m|^2$) of each focal point can be extracted from the FDTD () solutions. Then, the mean intensity of all focal points can be obtained from $|\bar{E}|^2 = \frac{\sum_{m=1}^{N} |E_m|^2}{N}$. When the condition of $1 - \Delta k < \frac{E_m}{\bar{E}} < 1 + \Delta k$ ($\Delta k = 0.05$ is the tolerance level) is satisfied, the iterative algorithm will jump out of the loop, while the parameter "A_m" will be updated as $A_m = A_m \pm \gamma * (\frac{E_m}{\bar{E}} - 1)$ ($\gamma = 0.5$ is a compensation coefficient or defined as iterative coefficient) until the condition $1 - \Delta k < \frac{E_m}{\bar{E}} < 1 + \Delta k$ is met. Here, all the optimization procedure is performed with a commercial software of FDTD (finite-different time-domain) solutions.

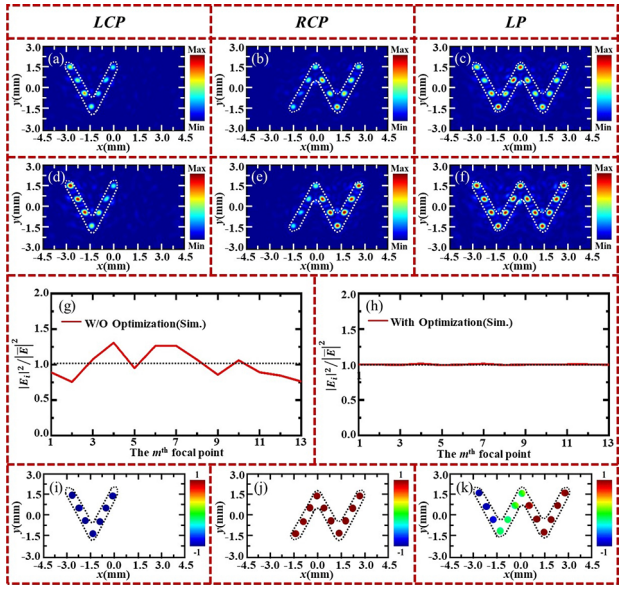

Fig. 2. Calculated electric-field intensity and polarization distributions of a metalens for generating a single-channel image consisting of CP- and LP-based focal points. (a)–(c)/(d)–(f) Electric-field intensity distributions of the multi-foci metalens without/with optimization under the illumination of LCP, RCP, and LP THz waves. (g) and (h) Intensity fluctuation for (c) and (f), respectively. (i)–(k) Polarization distributions for (d)–(f), respectively.

A multi-foci metalens can generate a multi-polarized image consisting of CP- and LP-based focal points, as shown in Fig. 2. The designed metalens consists of 80×80 meta-atoms (the more computing time with the increasing number of meta-atoms and vice versa), and the width, length, and height are $W = 35$ μm, $L = 100$ μm, $H_1 = 380$ μm, respectively. The period is $P = 120$ μm, and the thickness of the substrate is $H_2 = 620$ μm. Each meta-atom is considered as a quasi-half-wave plate [with the polarization conversion efficiency of 97% at 0.7 THz (working frequency)]. Each focal point is theoretically designed at 4 mm. Under the illumination of LCP THz waves, seven RCP focal points can be observed after the designed metalens, as shown in Fig. 2(a). Without the inverse design (without optimization), the intensity distributions of letter "V" consisting of seven RCP focal points are inhomogeneous. For the incidence of RCP THz waves, another letter "*N*" consisting of ten LCP focal points with inhomogeneous intensity distributions are observed after the designed metalens, as shown in Fig. 2(b). For the incidence of LP THz waves, the letters "V" and "*N*"are simultaneously generated and partially overlapped with each other, resulting in another letter "W"with the inhomogeneous intensity distributions and multiple polarizations [Fig. 2(c)]. The simulated intensity fluctuation of the total field (of letter "W") ranges from −24.31% to 30.9% (with respect to the mean value of these thirteen focal points), as shown in Fig. 2(g). For the optimized metalens, the letters "V"and "*N*" with the quantitative intensity

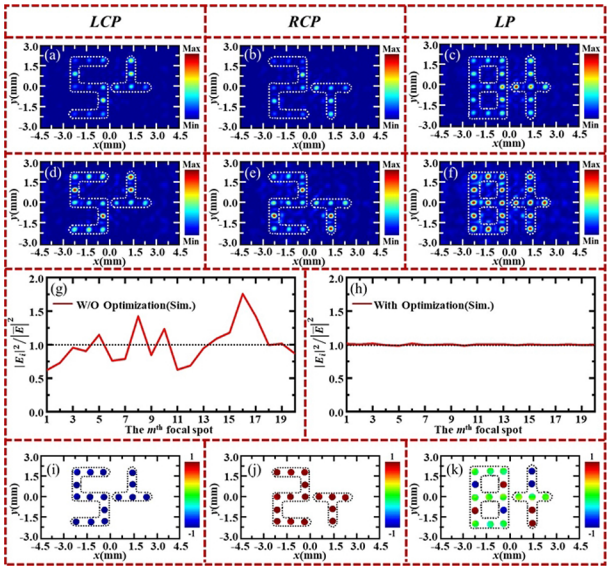

Fig. 3. Calculated electric-field intensity and polarization distributions of a metalens for generating a dual-channel image consisting of CP- and LP-based focal points. (a)–(c)/(d)–(f) Electric-field intensity distributions of the multi-foci metalens without/with optimization under the illumination of LCP, RCP, and LP THz waves. (g) and (h) Intensity fluctuation for (c) and (f), respectively. (i)–(k) Polarization distributions for (d)–(f), respectively.

distributions and the letter "W"with homogeneous intensity distributions are observed, as shown in Figs. 2(d)–2(f). It should be noted that the simulated intensity fluctuation of the total field (of letter "W") generated from the optimized metalens ranges from −0.81% to 1.09% [Fig. 2(h)], which is much smaller than that of the non-optimized case. The polarizations of the letters "V" and "*N*" are RCP and LCP states [Figs. 2(i) and 2(j)], respectively, while the letter "W" consists of LCP-, RCP-, and LP-based focal points [Fig. 2 (k)], leading to a multi-polarized image. The calculated diffraction-efficiency of this metalens is 36.44%. The sequence number and optimized amplitude of each focal point in "W" are given in Supplement 1, Fig. S1(a) and Table S1, respectively. A metalens that can generate focal points in three dimensions is also added into Supplement 1, as shown in Fig. S2.

Our proposed approach can be extended to designing metalens with multi-channel images consisting of multi-polarized focal points. As shown in Fig. 3(a) for the incident LCP THz waves, two images (i.e., "5" and an inverted letter "T") with inhomogeneous intensity distributions are observed. For the incidence of RCP THz waves, another two images of "2" and "T" with inhomogeneous intensity distributions are generated, as shown Fig. 3(b). Under the illumination of LP THz waves, two of these four images are simultaneously generated and partially overlapped with each other, leading to two new images of "8" and "†" with inhomogeneous intensity distributions in Fig. 3(c). The intensity fluctuation of "8" and "†" ranges from –38.5% to 74.6%, as shown in Fig. (g). However, for the optimized case, the images "5", inverted letter "T", "2" and "T" with quantitative intensity distributions are observed after the optimized metalens under the illumination of LCP/RCP THz waves, as shown in Figs. 3(d) and 3(e). Two new images of "8" and "†" with homogeneous intensity distribution [Fig. 3(f)] and the intensity fluctuation of these two images range from −1.35% to 1.07%. As shown in Figs. 3(i) and 3(j), the polarizations of the two images "5", inverted letter "T" are RCP states, while the polarizations of the two images of "2" and "T" are LCP states. In addition, the two images of "8" and "†"consist of LCP-, RCP-, and LP-based focal points with homogeneous intensity distributions [Fig. 3 (k)], demonstrating the multi-channel and multi-polarized images with uniform intensity distributions. The calculated diffraction-efficiency of this metalens is 36.37%. The sequence number and optimized amplitude of each focal point in "8" and "†" are given in Supplement 1, Fig. S1(b) and Table S2, respectively.

In order to verify our proposed approach, we fabricate a sample that can generate the letters "V", "*N*", and "W" under the illumination of LCP, RCP, and LP THz waves. Figure 4(a) shows the optical image of the inversely designed metalens. For the incidence of LCP and RCP THz waves, the letters "V" and "*N*" with the quantitative intensity distributions are observed after the designed metalens, as shown in Figs. 4(b) and 4(c). Under the illumination of LP THz waves, both of the letters "V" and "*N*" are generated and partially overlapped with each

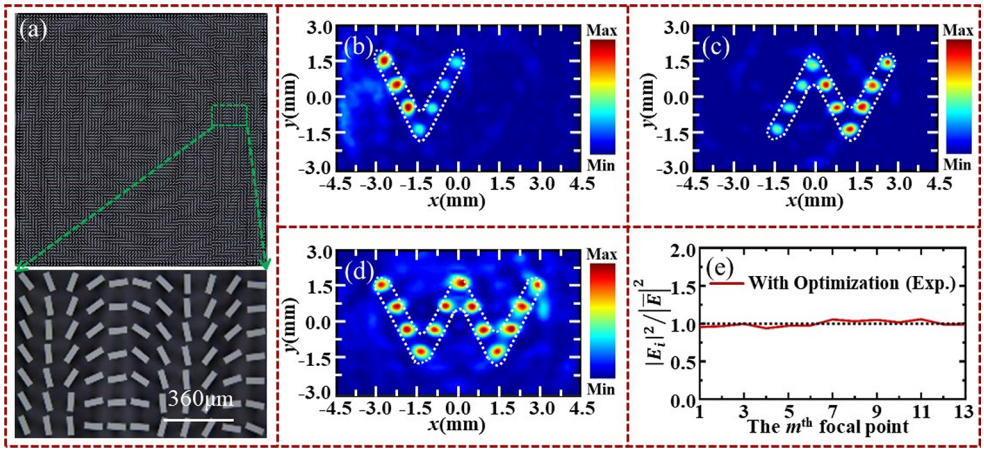

Fig. 4. Measured electric-field intensity and polarization distributions of a metalens for generating a single-channel image consisting of CP- and LP-based focal points. (a) Optical image of the fabricated sample. (b)–(d) Measured electric-field intensity distributions of the multi-foci metalens with optimization under the illumination of LCP, RCP and LP THz waves. (e) Measured intensity fluctuation of (d).

other, leading to a new letter "W" with nearly homogeneous intensity distributions, as shown in Fig. 4(d). The measured intensity fluctuation of the total field (of letter "W") ranges from −6.06% to 5.8% [Fig. 4(e)], which demonstrate that the generated letter "W" enables nearly homogeneous intensity distributions between each focal point. The background noise can be attributed to the fabrication errors and non-perfect decoherence. The measured diffraction-efficiency of this metalens is 27.6%.

In summary, an inverse design approach was proposed to optimize the in-plane orientation of each meta-atom in a multi-foci metalens to manipulate the field intensity of each focal point. By combining the modulation of polarization and intensity of each focal point, the single-/dual-channel and multi-polarized images consisting of a plethora of focal points with different polarizations but nearly identical intensity distributions have been obtained. It should be noted that the polarization-dependent images can be also realized by the traditional approach of computer-generated holography, but the generated focal points cannot enable the functionality in imaging. Our proposed approach for generating multiple focal points with uniform intensity distributions is based on the metalens, and each focal point is generated by the functionality of a lens. Such a robust approach can be extended to design other ultracompact devices with high-accuracy functionalities.

Funding. National Key Research and Development Program of China (2023YFF0719200); National Natural Science Foundation of China (61988102, 62271320); "Shuguang" Program of Shanghai Education Commission (19SG44); The Project from Science and Technology Commission of Shanghai Municipality (22JC1400200).

Disclosures. The authors declare no conflicts of interest.

Data availability. Data underlying the results can be obtained from the authors upon reasonable request.

Supplemental document. See Supplement 1 for supporting content.

REFERENCES

1. N. F. Yu, P. Genevet, M. A. Kats, *et al.*, Science **334**, 333 (2011).
2. L. L. Huang, X. Z. Chen, H. Muhlenbernd, *et al.*, Nano Lett. **12**, 5750 (2012).
3. N. K. Grady, J. E. Heyes, D. R. Chowdhury, *et al.*, Science **340**, 1304 (2013).
4. L. Q. Cong, N. N. Xu, J. Q. Gu, *et al.*, Laser Photonics Rev. **8**, 626 (2014).
5. X. F. Zang, F. L. Dong, F. Y. Yue, *et al.*, Adv. Mater. **30**, 1707499 (2018).
6. L. G. Deng, J. Deng, Z. Q. Guan, *et al.*, Light: Sci. Appl. **9**, 101 (2020).
7. M. Z. Liu, W. Q. Zhu, P. C. Huo, *et al.*, Light: Sci. Appl. **10**, 107 (2021).
8. X. Zhang, X. Li, H. Q. Zhou, *et al.*, Adv. Funct. Mater. **32**, 2209460 (2022).
9. R. X. Wang, J. Han, J. L. Liu, *et al.*, Opt. Lett. **45**, 3506 (2020).
10. X. Yin, Z. Ye, J. Rho, *et al.*, Science **339**, 1405 (2013).
11. W. J. Luo, S. Y. Xiao, Q. He, *et al.*, Adv. Opt. Mater. **3**, 1102 (2015).
12. X. F. Zang, B. S. Yao, Z. Li, *et al.*, Nanophotonics **9**, 1501 (2020).
13. X. H. Ling, Z. Zhang, Z. Dai, *et al.*, Laser Photonics Rev. **17**, 2200783 (2023).
14. B. Walther, C. Helgert, C. Rockstuhl, *et al.*, Adv. Mater. **24**, 6300 (2012).
15. H. Liu, M. Q. Mehmood, K. Huang, *et al.*, Adv. Opt. Mater. **2**, 1193 (2014).
16. X. J. Ni, A. V. Kildishev, and V. M. Shalaev, Nat. Commun. **4**, 2807 (2013).
17. G. X. Zheng, H. Mühlenbernd, M. Kenney, *et al.*, Nat. Nanotechnol. **10**, 308 (2015).
18. D. D. Wen, F. Y. Yue, G. X. Li, *et al.*, Nat. Commun. **6**, 8241 (2015).
19. L. Jin, Z. G. Dong, S. T. Mei, *et al.*, Nano Lett. **18**, 8016 (2018).
20. Q. Song, M. Odeh, J. Zúñiga-Pérez, *et al.*, Science **373**, 1133 (2021).
21. H. Wang, Z. Qin, L. L. Huang, *et al.*, PhotoniX **3**, 10 (2022).
22. X. Chen, L. Huang, H. Mühlenbernd, *et al.*, Nat. Commun. **3**, 1198 (2012).
23. A. Arbabi, Y. Horie, A. J. Ball, *et al.*, Nat. Commun. **6**, 7069 (2015).
24. M. Khorasaninejad, W. T. Chen, R. C. Devlin, *et al.*, Science **352**, 1190 (2016).
25. S. Wang, P. C. Wu, V. C. Su, *et al.*, Nat. Commun. **8**, 187 (2017).
26. W. T. Chen, A. Y. Zhu, V. Sanjeev, *et al.*, Nat. Nanotechnol. **13**, 220 (2018).
27. R. J. Lin, V.-C. Su, S. Wang, *et al.*, Nat. Nanotechnol. **14**, 227 (2019).
28. R. Wang, Y. Intaravanne, S. Li, *et al.*, Nano Lett. **21**, 2081 (2021).
29. X. W. Wang, H. Wang, J. L. Wang, *et al.*, Nat. Commun. **14**, 2063 (2023).
30. R. X. Wang, M. Ansari, H. Ahmed, *et al.*, Light: Sci. Appl. **12**, 103 (2023).
31. J. T. Hu, D. Q. Wang, D. Bhowmik, *et al.*, ACS Nano **13**, 4613 (2019).
32. Y. B. Ni, S. Chen, Y. J. Wang, *et al.*, Nano Lett. **20**, 6719 (2020).
33. S. Molesky, Z. Lin, A. Y. Piggott, *et al.*, Nat. Photonics **12**, 659 (2018).
34. W. T. Chen, A. D. Y. Zhu, and F. Capasso, Nat. Rev. Mater. **5**, 604 (2020).
35. E. Bayati, R. Pestourie, S. Colburn, *et al.*, ACS Photonics **7**, 873 (2020).
36. A. Y. Piggott, J. Lu, K. G. Lagoudakis, *et al.*, Nat. Photonics **9**, 374 (2015).
37. R. Pestourie, C. Pérez-Arancibia, Z. Lin, *et al.*, Opt. Express **26**, 33732 (2018).
38. D. Sell, J. J. Yang, S. Doshay, *et al.*, Nano Lett. **17**, 3752 (2017).
39. C. Lin, Y. Chen, J. T. Lin, *et al.*, Nano Lett. **21**, 4981 (2021).
40. S. An, B. Zheng, M. Y. Shalaginov, *et al.*, Adv. Opt. Mater. **10**, 2102133 (2022).